In vivo calcium imaging from dentate granule cells with wide-field fluorescence microscopy

Yuichiro Hayashi[1,2,3¤a]*, **Satoshi Yawata**[1¤b], **Kazuo Funabiki**[1¤c], **Takatoshi Hikida**[2¤d]

1 Osaka Bioscience Institute, Suita, Osaka, Japan, **2** Medical Innovation Center, Kyoto University Graduate School of Medicine, Kyoto, Japan, **3** Frontier Research Center for Post-genome Science and Technology, Hokkaido University, Sapporo, Japan

¤a Current address: Institute of Biomedical Sciences, Kansai Medical University, Hirakata, Osaka, Japan
¤b Current address: Department of Physiology, Kyoto University Graduate School of Medicine, Kyoto, Japan
¤c Current address: IBRI Laboratory, Foundation for Biomedical Research Innovation, Kobe, Hyogo, Japan
¤d Current address: Institute for Protein Research, Osaka University, Osaka, Japan
* hayashiy16@gmail.com

Abstract

A combination of genetically-encoded calcium indicators and micro-optics has enabled monitoring of large-scale dynamics of neuronal activity from behaving animals. In these studies, wide-field microscopy is often used to visualize neural activity. However, this method lacks optical sectioning capability, and therefore its axial resolution is generally poor. At present, it is unclear whether wide-field microscopy can visualize activity of densely packed small neurons at cellular resolution. To examine the applicability of wide-field microscopy for small-sized neurons, we recorded calcium activity of dentate granule cells having a small soma diameter of approximately 10 micrometers. Using a combination of high numerical aperture (0.8) objective lens and independent component analysis-based image segmentation technique, activity of putative single granule cell activity was separated from wide-field calcium imaging data. The result encourages wider application of wide-field microscopy in *in vivo* neurophysiology.

Introduction

To record neural activity in living animals, extracellular electrophysiological recording has been widely used [1–3]. This technique offers high temporal resolution and low invasion of brain tissue, but recording the same neurons for a long period of time (days to weeks) and to determine their precise location and cell types are difficult. In contrast, calcium imaging with genetically-encoded calcium indicators provides a long-term, cell-type-specific method of recording neural activity [4,5]. Because two-photon microscopy provides deep tissue penetration and optical sectioning capability, it is suitable for *in vivo* calcium imaging of deep brain structures. However, because each pixel in an image is sampled serially in two-photon microscopy, an inevitable tradeoff exists between the size of imaging area and frame rate. Two-photon microscope using wide-field excitation or multi-beam scanning technique offers wide field of view at high frame rate [6,7]. However, their applicability to *in vivo* calcium imaging is yet

to be demonstrated. On the other hand, wide-field microscopy have also been used for visualizing neural dynamics in various brain structures [8–12]. Unlike conventional two-photon microscopy, all pixels in an image are sampled simultaneously in wide-field microscopy. Therefore, this method is advantageous over two-photon microscopy for high speed, high resolution imaging. However, due to the lack of optical sectioning capability, axial resolution of wide-field microscopy is worse than that of confocal or two-photon microscopy. At present, it is unclear whether wide-field microscopy is applicable to densely packed small cells. To examine the applicability of wide-field fluorescence microscopy for smaller sized neurons, we recorded calcium activity of dentate granule cells (GCs) having a small soma diameter of approximately 10 micrometers. By employing high-numerical aperture (NA) (0.8) objective lens and independent component analysis (ICA)-based cell sorting technique, activity of individual hippocampal GCs in head-restrained mouse were separated.

Materials and methods

Optical path

A simplified schematic of the optical path is shown in Fig 1A. Excitation light was emitted from a blue LED (LXK2-PB14-P00; Lumileds, Aachen, Germany). The light passed through an excitation filter (FF480/40-25; Semrock, Rochester, NY) and then reflected by a dichroic mirror (FF506-Di02-25x36; Semrock) onto the tissue through a water-immersion objective lens (40×0.8NA; Olympus, Tokyo, Japan). Fluorescent emissions collected by the objective lens were passed through the dichroic mirror and an emission filter (FF535/50-25; Semrock). The fluorescence image, focused by a tube lens (Nikkor 50mm f/1.8D, Nikon, Tokyo, Japan), was captured by a CMOS camera (FL3-U3-13S2M-CS, FLIR Systems, Willsonville, OR). Detailed construction of the overhead fluorescence microscope unit is shown in S1 Fig.

Resolution measurements

To determine resolution values, lateral and axial intensity profiles of the 0.5 μm fluorescent bead (C14837, Thermo Fischer Scientific, Waltham, MA) images were fit to Gaussian curves. We determined the full-width-at-half-maximum (FWHM) of each curve fit.

Animals and surgery

All animal care and use was in accordance with the protocols approved by Hokkaido University institutional animal care and use committee (project license number: 16–0042). Adult male C57BL/6J mice (10–16 weeks of age) were anesthetized with isoflurane, and then injected with 0.1mg/kg buprenorphine. The skull was exposed, and a small hole (<0.5 mm) was made over the right hemisphere (1.5 mm lateral to the midline, 2.3 mm posterior to the bregma). AAV1-syn-GCaMP6f-WPRE (University of Pennsylvania vector core) was diluted to $5{\times}10^{12}$ particles/mL in phosphate-buffered saline (PBS), and 150 nL was injected into granular layer of the dentate gyrus (1.6 mm ventral from the brain surface). One week after the viral injection, the animal was anesthetized and a 1.9 mm diameter craniotomy was performed. The dura was removed, and the underlying cortex and CA1 was aspirated. A stainless-steel cannula (1.81 mm outer diameter, 1.45 mm inner diameter, 1.8 mm height) covered by a cover glass (0.12 mm thickness) was inserted over the dorsal dentate gyrus. A titanium head plate (25×10 mm, 1mm thickness) and the skull were glued with dental cement (Shofu, Kyoto, Japan).
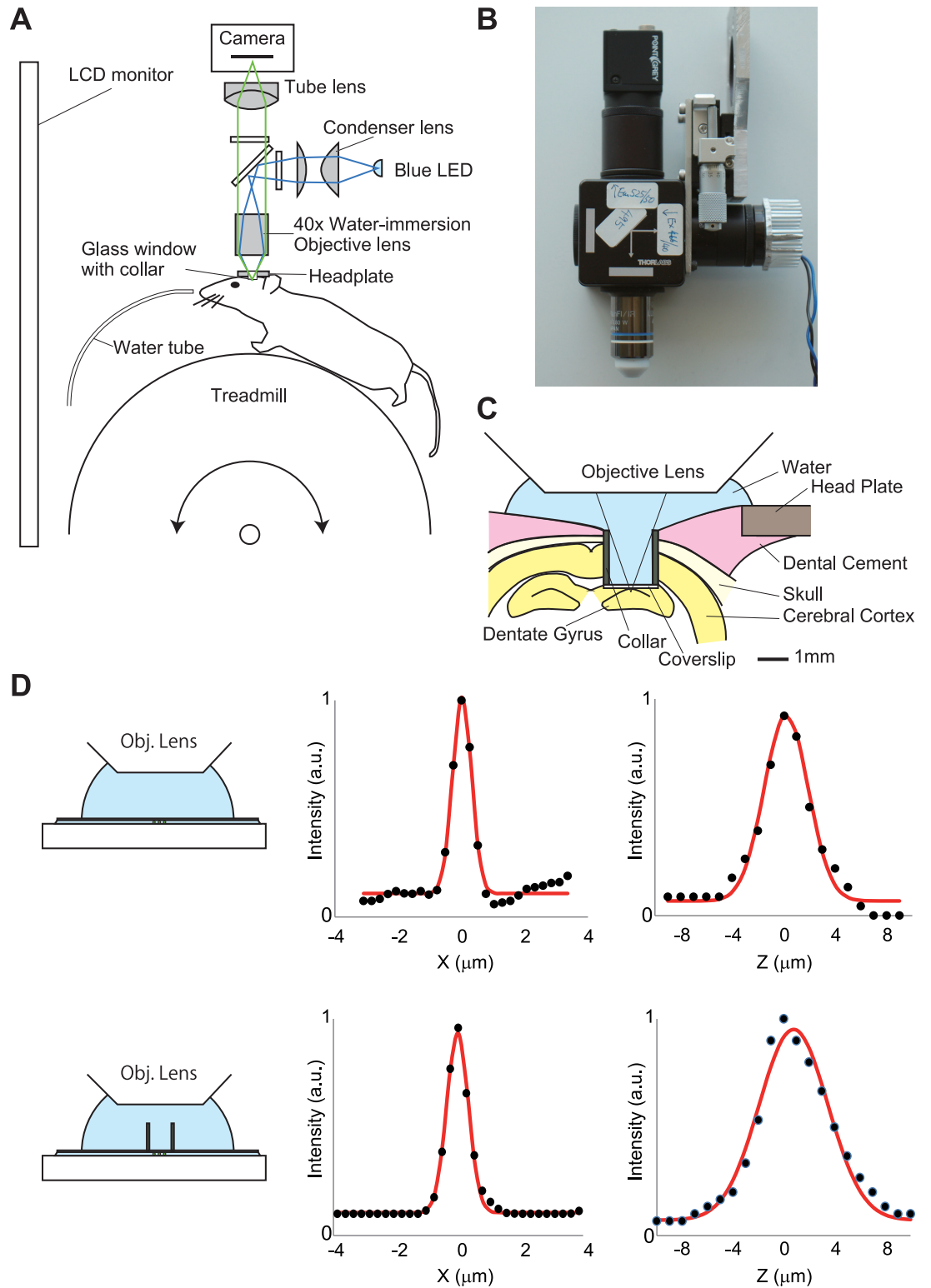
Fig 1. Wide-field imaging system for an awake head-restrained mouse. (A) Simplified schematic of the endoscope imaging system. The blue line indicates the illumination pathway and the green line indicates the light collection pathway. Illumination light from a blue LED was collected with a condenser lens, passes through an excitation filter, reflects off a dichroic mirror, and irradiated through an objective lens. The fluorescence image was focused on a CMOS

camera. (B) Image of the endoscope system. (C) Schematic of experimental setup showing the chronic window implant above the dentate gyrus. (D) Point spread function of the imaging setup with (lower) and without (upper) the cannula. Lateral (center) and axial (right) intensity line profiles across a 0.5 μm fluorescent bead (black dots) were shown. The read lines indicate Gaussian fits.

https://doi.org/10.1371/journal.pone.0180452.g001

VR system

A 24 inch LCD monitor (2407WFP, Dell, Round Rock, TX) placed ~26 cm from the mouse's head, and the VR environment image displayed on the monitor covered 90° and 77° of the mouse's horizontal and vertical field of view, respectively (Fig 2A). Mice were head-restrained with their limbs resting on a freely rotating treadmill consisting of a 20 cm diameter Styrofoam ball with a metal shaft. Ball rotations associated with mouse locomotion were read at 60 Hz with a computer mouse (G300, Logitech, Lausanne, Switzerland) placed under the ball. The length of the virtual track was 1.8 m. Mice received a small sugar water reward in an unmarked reward zone (1.5 m from the start point of the track) (Fig 2B). Once the mice reached the end of the track, they were teleported back to the start of the track. The Blender Game Engine (www.blender.org) and its Python interface were used to generate the VR environment.
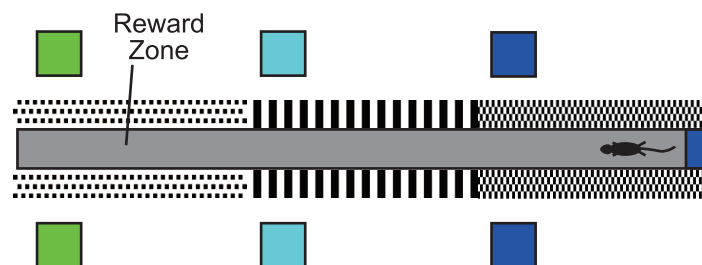
A
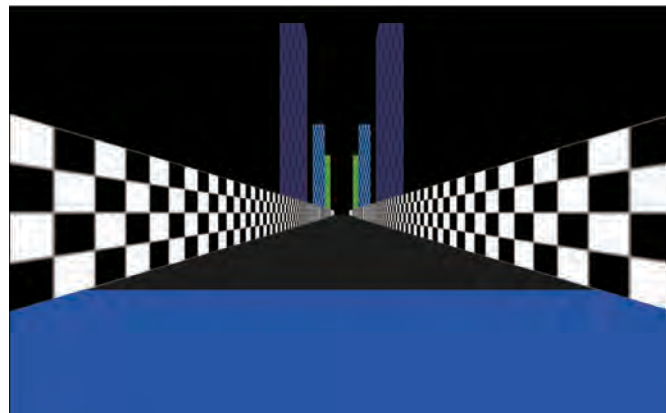
B

Fig 2. VR system for mice. (A) View from start point of the virtual linear track. (B) Top view of the track. Scale bar, 10 cm.

https://doi.org/10.1371/journal.pone.0180452.g002

Behavioral training

At least 2 week after the cranial window implantation, the mice underwent water restriction (2 mL per day), and training in the virtual linear track (two 5 min session per day) began. After 3–4 weeks of training, mice achieving a high performance levels (8 rewards per session) were used for recording session.

Imaging session

Excitation light intensity was approximately 0.04 mW/mm^2. Images were captured using Fly-Capture2 software (FLIR Systems, Willsonville, OR) at 10 Hz for 5 minutes.

Image processing

We used ImageJ1.49q (National Institute of Health) and MATLAB 2013a (Mathworks, Natick, MA) for all analyses. We first applied a spatial down-sampling of 4× to the image cropped to the area containing the putative neural activity. Then we corrected lateral displacements of the brain by image translation using TurboReg [13]. We used an averaged image of the entire frames as a reference for image alignment. Spatial filters corresponding to individual cells were identified using a PCA and ICA-based algorithm (Cellsort 1.0) (Mukamel et al., 2009).

Calcium activity data analysis

Ca^{2+} activity was extracted by applying the spatial filters to the time-lapse image. The Ca^{2+} transients were identified by searching each trace for local maxima that had a peak amplitude of more than 3× standard deviation from the baseline (defined as the average of the trace calculated across the entire sessions).

Results

Wide-field fluorescence imaging of dentate GCs in awake behaving mice

To test the feasibility of wide-field microscopy for *in vivo* calcium imaging from small, densely packed neurons, we record activity from GCs of the dentate gyrus. These cells have small soma (approximately 10 μm) and are tightly packed in the granular layer [14], therefore, imaging optics should have high lateral and axial resolution. In *in vivo* calcium imaging with wide field fluorescence microscopy, gradient refractive index (GRIN) lens is often used as objective lens. However, because of its low NA (<0.6) and significant optical aberrations, the optical resolution of singlet GRIN lens is not as good as conventional microscope objectives. To achieve high axial resolution, we used a 40×, 0.8NA water-immersion objective lens (Fig 1A and 1B). The lateral and axial full-width at half-maximum (FWHM) of the point spread function was 0.70 μm and 4.03 μm (Fig 1D, upper). For *in vivo* imaging from dentate gyrus, we used glass window with stainless-steel cannula (Fig 1C). Because the cannula blocks light rays of the object, effective numerical aperture is reduced to ~0.5, which impairs the spatial resolution. Therefore, we also measured PSF in the presence of the cannula. The lateral and axial FWHM are 0.81μm and 6.36 μm, respectively, which are less than soma size of the GCs (Fig 1D, lower). To test whether this imaging setup can resolve individual GCs, three-dimensional image of formaldehyde-fixed brain tissue expressing GCaMP6f [15] at 2 μm step, and multiple XZ views were shown (S2 Fig). In each XZ plane contains one or more GCaMP6f-labeled neurons, and the shape of individual neurons were clearly visualized (S2 Fig). These results suggest that the spatial resolution of this imaging setup is sufficient for cellular-level calcium imaging of dentate GCs. However, unlike confocal or two-photon microscopy, fluorescence from out-of-focus plane is also received by the image sensor in wide-field microscopy. Therefore, each

pixel in the image obtained by this method can contain a mixture of signals from multiple cells [16]. This mixed signal can be separated into signal from individual cells using statistical techniques [17–20]. We used principal and independent component analysis (PCA and ICA)-based method (Cellsort)[17] for cell sorting.

The mouse was head-fixed on a spherical treadmill that allows the mouse to run freely (Fig 1A) [21]. A custom virtual-reality (VR) system for rodents [22–25] was used to present spatial cues. A liquid crystal display (LCD) monitor installed in front of the mouse displayed a computer-generated image of a virtual linear track (Fig 2).

Mice were injected with an adeno-associated virus (AAV) expressing GCaMP6f into the granular layer of the dentate gyrus, and then implanted with a glass window. After 2–4 week of recovery, mice were trained to obtain a sugar water reward (10% sucrose, 4 µL) at a hidden goal zone in the virtual linear track.

Activity profile of the dentate GCs

We recorded fluorescent images from the dentate gyrus at 10 Hz for 5 min while mice were performing the VR task (running speed: 2.2 ± 0.96 cm/s, reward rate: 10.0 ± 4.8 reward/session, mean ± SEM, n = 4)(Fig 3A, S1 File). We then extracted fluorescent signals of individual cells from the image data using Cellsort program (Mukamel et al., 2009). The shape and size of spatial filters derived by ICA suggested that the method successfully identified individual cells (Fig 3B). We then applied these spatial filters to extract individual calcium activity profiles, and detected calcium transients from the extracted waveform (Fig 3C). Of 967 cells (n = 4 mice) detected by ICA, calcium activity of the GCs was very sparse (0.17 ± 0.0057 events/min, mean ± SEM), which is consistent with previous *in vivo* calcium imaging studies using two-photon microscopy [26,27].

Discussion

Wide-field microscopy have been used to image calcium activity in various brain regions from awake behaving animals [10–12]. Noteworthy, owing to its simple mechanism, the method can be miniaturized for imaging from free-moving rodents, which have expanded the scope of applications [12]. A major disadvantage of wide-field microscopy is lacking of optical sectioning capability, and hence poor axial resolution. To separate individual activity of small, densely packed cells, we first used high-NA (0.8) objective lens. This lens yielded high lateral and axial resolution, which is enough to separate individual dentate GCs (Fig 1D and S2 Fig). Second, we used PCA-ICA based cell sorting software (Cellsort)[17] (Fig 3B) to separate overlapping fluorescence from adjacent cells. Spatial filters derived from the software appear to represent individual GCs with minimal overlap (Fig 3B), suggesting that the software successfully extracted individual cell activity. Activity traces of the dentate GCs during rest and running on the treadmill were highly sparse (Fig 3C), consistent with previous electrophysiological studies [26,28–31] and calcium imaging studies [26,27]. The two calcium imaging studies using two-photon microscopy observed extremely low calcium transient rate (0.1~0.5 events/min) [26,27]. Our present result (0.17 events/min) was in the range of previously reported values, also indicating that our method successfully extracted calcium activity at cellular resolution. We did not analyzed place-related activity of the GCs, because we did not collect sufficient number of calcium transient for reliable estimation of place field in a recording session (5 min), owing to their extremely low calcium transient rate. Much longer recording time is needed to determine place field properties of the dentate GCs.

In this work we used conventional optical components and a low-cost, general purpose CMOS camera at a cost of about 500 USD (Fig 1A and 1B and S1 Fig). This system exhibited
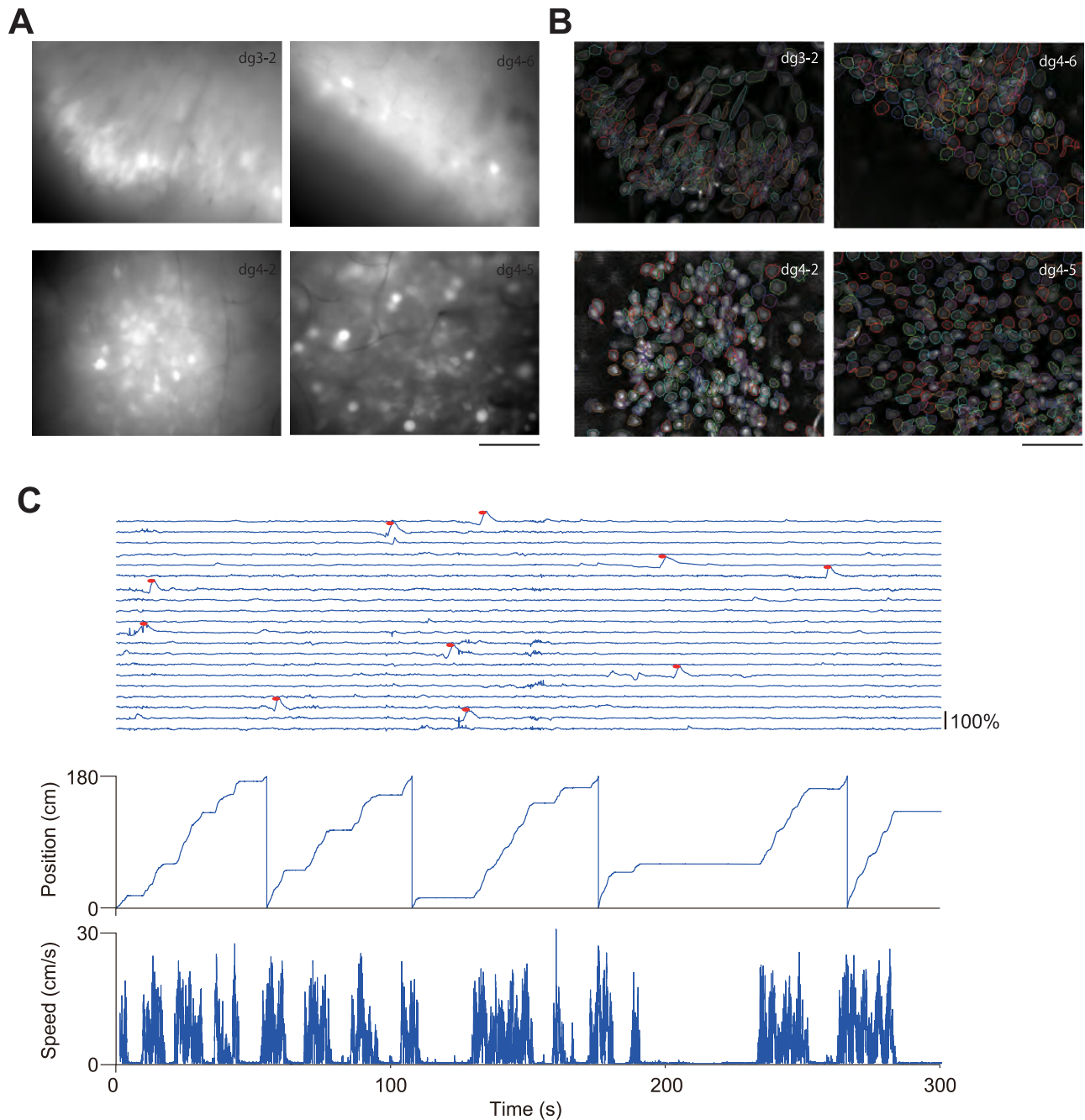
Fig 3. Imaging the dentate gyrus in behaving mice. (A) Averaged fluorescence images across entire recording session. Scale bar, 100 μm. (B) Contours of putative cell bodies identified with a PCA and ICA-based cell sorting algorithm (Cellsort 1.0, Mukamel et al., 2009). Scale bar, 100 μm. (C) Traces of dF/F calcium signal were shown. Identified calcium transients are shown as red dots. The position of the mouse along the virtual track is shown at the bottom. Animal position and speed in the virtual track was shown in the bottom.

sufficient performance for *in vivo* calcium imaging of dentate GCs (Fig 3). However, instead of the low-cost camera used in this study, high sensitivity, low noise cameras, such as cooled CMOS cameras or electron-multiplying charge coupled device (EM-CCD) cameras, enable a higher frame rate and longer recording time [11].

An important application of wide-field microscopy in neuroscience is head-mount fluorescent microscope for rodents [12]. Because of its small size (~2g), imaging optics should be simple and small-size. Therefore, in most cases, GRIN lens is used as objective lens. However, due to its low NA (<0.6) and optical aberrations, the resolution is not as good as conventional microscope objectives. To improve image quality of GRIN lens-based imaging system, compound lens system [32] or adding correction optics [33] have been proposed. The former type of GRIN lens–based, high NA (0.8) probe have been commercially available (GRINTECH GmbH, Jena, Germany). The probe is small diameter (1 mm) and offers diffraction-limited spatial resolution. Due to its small diameter, the probe can be implanted in animal's brain. Therefore it is suitable for visualization of deep brain structures. One shortcoming of the probe is narrow field of view (~75 μm diameter)[34]. On the other hand, our method offers larger field of view (~1 mm for our present implementation). However, imaging depth is restricted by the working distance of the objective lens located outside the brain tissue. Overall, these two methods are complementary to each other.

The optical path of our imaging system (Fig 1B) is easily expandable to dual-color imaging. This modification will allow dual-color imaging of various förster resonance energy transfer (FRET) biosensors [35–37] or dual-color calcium imaging [38]. Overall, the low cost, easy-to-build high-resolution imaging system described here would facilitate research using deep brain functional imaging of behaving animals.

Supporting information

S1 Fig. Schematic diagram of the custom wide-field fluorescent microscope. Mechanical and optical components necessary to construct the microscope were shown.
(PDF)

S2 Fig. XY and XZ views of a formaldehyde-fixed mouse brain expressing GCaMP6f. Eighty XY images were taken with intervals of 2 μm (Top) and a 3D tissue volume was reconstructed from the fluorescence images. XY (Bottom, left) and XZ (Bottom, right) views of the 3D tissue volume were shown.
(PDF)

S1 File. Example movie of calcium imaging from dentate gyrus. An example of dF/F format data recorded from the dentate gyrus in a mouse running along a virtual track (animal id:dg4-2). The calcium imaging data was acquired at 10 fps and the movie is displayed at 30 fps. dF/F was calculated as follows; dF/F = (F(t)-F0)/F0, where F0 is the mean image obtained by averaging the entire movie, and F(t) is every frame in the movie.
(AVI)

S2 File. ARRIVE guidelines. NC3Rs ARRIVE guidelines checklist.
(DOCX)

Acknowledgments

Author Contributions

Conceptualization: YH.

Data curation: YH.

Formal analysis: YH.

Funding acquisition: YH TH.

Investigation: YH TH.

Methodology: YH SY KF.

Project administration: YH.

Resources: YH SY.

Software: YH.

Supervision: YH.

Validation: YH.

Visualization: YH.

Writing – original draft: YH.

Writing – review & editing: YH SY KF TH.

References

1. Evarts E V. Pyramidal tract activity associated with a conditioned hand movement in the monkey. J Neurophysiol. 1966/11/01. 1966; 29: 1011–1027. Available: http://www.ncbi.nlm.nih.gov/pubmed/4961643 PMID: 4961643

2. Hubel DH, Wiesel TN. Receptive fields of single neurones in the cat's striate cortex. J Physiol. 1959/10/01. 1959; 148: 574–591. Available: http://www.ncbi.nlm.nih.gov/pubmed/14403679 PMID: 14403679

3. O'Keefe J, Dostrovsky J. The hippocampus as a spatial map. Preliminary evidence from unit activity in the freely-moving rat. Brain Res. 1971; 34: 171–175. Available: http://www.ncbi.nlm.nih.gov/entrez/query.fcgi?cmd=Retrieve&db=PubMed&dopt=Citation&list_uids=5124915 PMID: 5124915

4. Huber D, Gutnisky DA, Peron S, O'Connor DH, Wiegert JS, Tian L, et al. Multiple dynamic representations in the motor cortex during sensorimotor learning. Nature. 2012/04/28. 2012; 484: 473–478. https://doi.org/10.1038/nature11039 PMID: 22538608

5. Kerlin AM, Andermann ML, Berezovskii VK, Reid RC. Broadly tuned response properties of diverse inhibitory neuron subtypes in mouse visual cortex. Neuron. 2010; 67: 858–71. https://doi.org/10.1016/j.neuron.2010.08.002 PMID: 20826316

6. Niesner R, Andresen V, Neumann J, Spiecker H, Gunzer M. The Power of Single and Multibeam Two-Photon Microscopy for High-Resolution and High-Speed Deep Tissue and Intravital Imaging. Biophys J. 2007; 93: 2519–2529. https://doi.org/10.1529/biophysj.106.102459 PMID: 17557785

7. Oron D, Tal E, Silberberg Y. Scanningless depth-resolved microscopy. Opt Express. Optical Society of America; 2005; 13: 1468. https://doi.org/10.1364/OPEX.13.001468

8. Jennings JH, Ung RL, Resendez SL, Stamatakis AM, Taylor JG, Huang J, et al. Visualizing hypothalamic network dynamics for appetitive and consummatory behaviors. Cell. 2015/01/31. 2015; 160: 516–527. https://doi.org/10.1016/j.cell.2014.12.026 PMID: 25635459

9. Betley JN, Xu S, Cao ZFH, Gong R, Magnus CJ, Yu Y, et al. Neurons for hunger and thirst transmit a negative-valence teaching signal. Nature. Nature Publishing Group, a division of Macmillan Publishers Limited. All Rights Reserved.; 2015; 521: 180–185. https://doi.org/10.1038/nature14416 PMID: 25915020

10. Ziv Y, Burns LD, Cocker ED, Hamel EO, Ghosh KK, Kitch LJ, et al. Long-term dynamics of CA1 hippocampal place codes. Nat Neurosci. 2013/02/12. 2013; 16: 264–266. https://doi.org/10.1038/nn.3329 PMID: 23396101

11. Mohammed AI, Gritton HJ, Tseng H-A, Bucklin ME, Yao Z, Han X. An integrative approach for analyzing hundreds of neurons in task performing mice using wide-field calcium imaging. Sci Rep. 2016; 6: 20986. https://doi.org/10.1038/srep20986 PMID: 26854041

12. Ghosh KK, Burns LD, Cocker ED, Nimmerjahn A, Ziv Y, Gamal AE, et al. Miniaturized integration of a fluorescence microscope. Nat Methods. 2011/09/13. 2011; 8: 871–878. https://doi.org/10.1038/nmeth.1694 PMID: 21909102

13. Thévenaz P, Ruttimann UE, Unser M. A pyramid approach to subpixel registration based on intensity. IEEE Trans Image Process. 1998; 7: 27–41. https://doi.org/10.1109/83.650848 PMID: 18267377

14. Claiborne BJ, Amaral DG, Cowan WM. Quantitative, three-dimensional analysis of granule cell dendrites in the rat dentate gyrus. J Comp Neurol. 1990; 302: 206–219. https://doi.org/10.1002/cne.903020203 PMID: 2289972

15. Chen TW, Wardill TJ, Sun Y, Pulver SR, Renninger SL, Baohan A, et al. Ultrasensitive fluorescent proteins for imaging neuronal activity. Nature. 2013/07/23. 2013; 499: 295–300. https://doi.org/10.1038/nature12354 PMID: 23868258

16. Hamel EJ, Grewe BF, Parker JG, Schnitzer MJ. Cellular Level Brain Imaging in Behaving Mammals: An Engineering Approach. Neuron. 2015/04/10. 2015; 86: 140–159. https://doi.org/10.1016/j.neuron.2015.03.055 PMID: 25856491

17. Mukamel EA, Nimmerjahn A, Schnitzer MJ. Automated analysis of cellular signals from large-scale calcium imaging data. Neuron. 2009/09/26. 2009; 63: 747–760. https://doi.org/10.1016/j.neuron.2009.08.009 PMID: 19778505

18. Pnevmatikakis EA, Soudry D, Gao Y, Machado TA, Merel J, Pfau D, et al. Simultaneous Denoising, Deconvolution, and Demixing of Calcium Imaging Data. Neuron. 2016; 89: 285–299. https://doi.org/10.1016/j.neuron.2015.11.037 PMID: 26774160

19. Maruyama R, Maeda K, Moroda H, Kato I, Inoue M, Miyakawa H, et al. Detecting cells using non-negative matrix factorization on calcium imaging data. Neural Networks. 2014; 55: 11–19. https://doi.org/10.1016/j.neunet.2014.03.007 PMID: 24705544

20. Vogelstein JT, Packer AM, Machado TA, Sippy T, Babadi B, Yuste R, et al. Fast nonnegative deconvolution for spike train inference from population calcium imaging. J Neurophysiol. American Physiological Society; 2010; 104: 3691–704. https://doi.org/10.1152/jn.01073.2009 PMID: 20554834

21. Dombeck DA, Khabbaz AN, Collman F, Adelman TL, Tank DW. Imaging large-scale neural activity with cellular resolution in awake, mobile mice. Neuron. 2007; 56: 43–57. https://doi.org/10.1016/j.neuron.2007.08.003 PMID: 17920014

22. Dombeck DA, Harvey CD, Tian L, Looger LL, Tank DW. Functional imaging of hippocampal place cells at cellular resolution during virtual navigation. Nat Neurosci. 2010/10/05. 2010; 13: 1433–1440. https://doi.org/10.1038/nn.2648 PMID: 20890294

23. Holscher C, Schnee A, Dahmen H, Setia L, Mallot HA. Rats are able to navigate in virtual environments. J Exp Biol. 2005/01/27. 2005; 208: 561–569. https://doi.org/10.1242/jeb.01371 PMID: 15671344

24. Harvey CD, Collman F, Dombeck DA, Tank DW. Intracellular dynamics of hippocampal place cells during virtual navigation. Nature. 2009/10/16. 2009; 461: 941–946. https://doi.org/10.1038/nature08499 PMID: 19829374

25. Youngstrom IA, Strowbridge BW. Visual landmarks facilitate rodent spatial navigation in virtual reality environments. Learn Mem. 2012; 19: 84–90. https://doi.org/10.1101/lm.023523.111 PMID: 22345484

26. Danielson NB, Kaifosh P, Zaremba JD, Lovett-Barron M, Tsai J, Denny CA, et al. Distinct Contribution of Adult-Born Hippocampal Granule Cells to Context Encoding. Neuron. 2016; 90: 101–12. https://doi.org/10.1016/j.neuron.2016.02.019 PMID: 26971949

27. Pilz G-A, Carta S, Stäuble A, Ayaz A, Jessberger S, Helmchen F. Functional Imaging of Dentate Granule Cells in the Adult Mouse Hippocampus. J Neurosci. Society for Neuroscience; 2016; 36: 7407–14. https://doi.org/10.1523/JNEUROSCI.3065-15.2016 PMID: 27413151

28. Alme CB, Buzzetti RA, Marrone DF, Leutgeb JK, Chawla MK, Schaner MJ, et al. Hippocampal granule cells opt for early retirement. Hippocampus. 2010; 20: 1109–23. https://doi.org/10.1002/hipo.20810 PMID: 20872737

29. Leutgeb JK, Leutgeb S, Moser MB, Moser EI. Pattern separation in the dentate gyrus and CA3 of the hippocampus. Science (80-). 2007; 315: 961–966. Available: http://www.ncbi.nlm.nih.gov/entrez/query.fcgi?cmd=Retrieve&db=PubMed&dopt=Citation&list_uids=17303747

30. Neunuebel JP, Knierim JJ. Spatial firing correlates of physiologically distinct cell types of the rat dentate gyrus. J Neurosci. 2012/03/17. 2012; 32: 3848–3858. https://doi.org/10.1523/JNEUROSCI.6038-11.2012 PMID: 22423105

31. Jung MW, McNaughton BL. Spatial selectivity of unit activity in the hippocampal granular layer. Hippocampus. 1993; 3: 165–82. https://doi.org/10.1002/hipo.450030209 PMID: 8353604

32. Barretto RPJ, Messerschmidt B, Schnitzer MJ. In vivo fluorescence imaging with high-resolution microlenses. Nat Methods. NIH Public Access; 2009; 6: 511–2. https://doi.org/10.1038/nmeth.1339 PMID: 19525959

33. Murray TA, Levene MJ. Singlet gradient index lens for deep in vivo multiphoton microscopy. J Biomed Opt. International Society for Optics and Photonics; 2012; 17: 21106. https://doi.org/10.1117/1.JBO.17.2.021106 PMID: 22463024

34. Barretto RPJ, Schnitzer MJ. In vivo optical microendoscopy for imaging cells lying deep within live tissue. Cold Spring Harb Protoc. Cold Spring Harbor Laboratory Press; 2012; 2012: 1029–34. https://doi.org/10.1101/pdb.top071464 PMID: 23028071

35. Miyawaki A, Llopis J, Heim R, McCaffery JM, Adams JA, Ikura M, et al. Fluorescent indicators for Ca2+ based on green fluorescent proteins and calmodulin. Nature. 1997; 388: 882–7. https://doi.org/10.1038/42264 PMID: 9278050

36. Goto A, Nakahara I, Yamaguchi T, Kamioka Y, Sumiyama K, Matsuda M, et al. Circuit-dependent striatal PKA and ERK signaling underlies rapid behavioral shift in mating reaction of male mice. Proc Natl Acad Sci U S A. 2015; 112: 6718–23. https://doi.org/10.1073/pnas.1507121112 PMID: 25964359

37. Yamaguchi T, Goto A, Nakahara I, Yawata S, Hikida T, Matsuda M, et al. Role of PKA signaling in D2 receptor-expressing neurons in the core of the nucleus accumbens in aversive learning. Proc Natl Acad Sci U S A. 2015; 112: 11383–8. https://doi.org/10.1073/pnas.1514731112 PMID: 26305972

38. Inoue M, Takeuchi A, Horigane S, Ohkura M, Gengyo-Ando K, Fujii H, et al. Rational design of a high-affinity, fast, red calcium indicator R-CaMP2. Nat Methods. Nature Publishing Group, a division of Macmillan Publishers Limited. All Rights Reserved.; 2015; 12: 64–70. https://doi.org/10.1038/nmeth.3185 PMID: 25419959